

Density of states in graphene with vacancies: midgap power law and frozen multifractality

V. Häfner,^{1,2} J. Schindler,^{1,2} N. Weik,^{1,2} T. Mayer,^{1,2} S. Balakrishnan,³ R. Narayanan,³ S. Bera,⁴ and F. Evers^{1,2,5}

¹ *Institute of Nanotechnology, Karlsruhe Institute of Technology, Campus North, D-76344 Karlsruhe, Germany*

² *Institut für Theorie der Kondensierten Materie,*

Karlsruhe Institute of Technology, Campus South, D-76128 Karlsruhe, Germany

³ *Department of Physics, Indian Institute of Technology Madras, Chennai 600036, India*

⁴ *Institute Néel and Université Grenoble Alpes, F-38042 Grenoble, France*

⁵ *Center of Functional Nanostructures, Karlsruhe Institute of Technology, Campus South, D-76131 Karlsruhe, Germany*

(Dated: January 16, 2022)

The density of states (DoS), $\varrho(E)$, of graphene is investigated numerically and within the self-consistent T-matrix approximation (SCTMA) in the presence of vacancies within the tight binding model. The focus is on compensated disorder, where the concentration of vacancies, n_A and n_B , in both sub-lattices is the same. Formally, this model belongs to the chiral symmetry class BDI. The prediction of the non-linear sigma-model for this class is a Gade-type singularity $\varrho(E) \sim |E|^{-1} \exp(-|\log(E)|^{-1/x})$. Our numerical data is compatible with this result in a preasymptotic regime that gives way, however, at even lower energies to $\varrho(E) \sim E^{-1} |\log(E)|^{-\mathfrak{r}}$, $1 \leq \mathfrak{r} < 2$. We take this finding as an evidence that similar to the case of dirty d-wave superconductors, also generic bipartite random hopping models may exhibit unconventional (strong-coupling) fixed points for certain kinds of randomly placed scatterers if these are strong enough. Our research suggests that graphene with (effective) vacancy disorder is a physical representative of such systems.

PACS numbers: 73.22.Pr, 72.80.Vp, 71.23.-k

Graphene is a hot topic in material sciences and condensed matter physics [1]. The material is interesting its electronic structure hosts two Dirac-cones. Since only the π_z -orbitals make significant contributions to the relativistic sectors of the band-structure, a tight-binding description of the material is frequently employed that keeps a single orbital per carbon atom and only nearest-neighbor hopping. Within this description it is easy to see that disorder introduced by a random distribution of vacancies has nontrivial effects. For instance, it is well known that a single impurity populates a mid-gap state which is power-law localized [2, 3]. With a finite concentration of vacancies a rich plethora of new phenomena emerges. One distinguishes the “compensated” case, – same concentration of vacancies in each sub-lattice, $\bar{n}=n_A=n_B$ – from the uncompensated case, $n_A > n_B$. In the latter case, one expects that the DoS exhibits a (pseudo-) gap, while for compensated disorder a sharp peak is observed [1]. Most studies focus on the balanced case at concentrations well below the percolation threshold, $\bar{n} \lesssim 30\%$. At present only very few aspects have been investigated in detail, despite the importance of the DoS for transport and optical properties of the functionalized material [4, 5].

Graphene with vacancies represents a bipartite random hopping system with time reversal and spin rotational invariance. Following the Zirnbauer-Altland classification of disordered metals it belongs to symmetry class BDI, [6, 7]. In the presence of weak bond disorder, a description based on the non-linear σ -model predicts for the density of states

$$\ln |E\varrho(E)| \sim -|\ln(E/\mathfrak{D})|^{1/x}, \quad |E| \lesssim \mathfrak{D} \quad (1)$$

where $\mathfrak{D}(\bar{n})$ denotes a microscopic energy scale. [7] The exponent $1/x$ reflects a peculiar feature of the RG-flow found by Gade and Wegner in a perturbative renormalization group (RG) study [8, 9]. Their analysis shows that the energy flow with the RG-scale L is $|\ln \epsilon| \propto z(L) |\ln L|$. Unlike the case with conventional critical behavior, the dynamical exponent z is not a constant here but rather $z(L) \propto \ln L$, so $|\ln \epsilon| \propto |\ln L|^2$ and correspondingly an exponent $x=2$ was obtained [31].

Later it was argued that the logarithmically growing exponent z is an indication of “freezing” [10, 11]. Freezing sets in when disorder has become so strong that critical wavefunctions concentrate in rare regions of the sample with very weak, power law tails leaking out of these “optimal” domains. In such situations, observables that derive from moments of wavefunction amplitudes higher than the first one cease to be sensitive to the sample geometry, so that their “flow” with the system size is “frozen”. Freezing implies that at $z \geq 3$ rare events dominate the energy-scaling and a new dependency $z \approx 4\sqrt{\ln L} - 1$ sets in [7]. As a consequence, the Gade-exponent $x=2$ gives way to $x=3/2$ and the zero-energy singularity becomes slightly *weaker* in the frozen limit.

A strong increase of the DoS near zero energy has been observed in several numerical works [3, 5, 12–14], but a quantitative check of the prediction, Eq. (1), is still missing. Here, we present such an analysis. We confirm the existence of a parametrically wide energy window where $\varrho(E)$ indeed follows Eq. (1). However, at ultra-low energies, Eq. (1) is not valid. Instead, the DoS crosses over to new behavior with a significantly *stronger* singularity, $1/(|E| \log(E)|^{\mathfrak{r}})$, with $2 > \mathfrak{r} \geq 1$.

Model and Methods (MaM): SCTMA. For the SCTMA we adopt the formalism developed in an earlier work and use it here to calculate the DoS [4, 15].

MaM: Stochastic time evolution. The SCTMA results are then compared against numerical simulation data for $\varrho(E)$ as obtained from a tight-binding Hamiltonian of the honeycomb lattice $\hat{H} = -t \sum_{\langle ij \rangle} c_i^\dagger c_j$ where as usual $\langle ij \rangle$ indicates nearest neighbor hopping. The disorder average is performed at vacancy concentration \bar{n} fixed and the same for both sublattices. We employ a numerical technique similar to Ref. [12] exploiting $\varrho(E) = \int_{-\infty}^{\infty} d\tau \varrho(\tau) e^{iE\tau}$ with the exact stochastic representation

$$\varrho(\tau) = \frac{1}{2\pi} \overline{\left\{ \langle \phi | \exp(-i\hat{H}\tau) | \phi \rangle \right\}_{\text{in}}}. \quad (2)$$

Here, $|\phi\rangle$ represents a random initial state and $\{\dots\}_{\text{in}}$ denotes an ensemble average of such states. For the evaluation of the matrix element we employ a standard Krylov-subspace approach, with a conservative choice of the width of the integration steps, typically $dt=0.01$ (units: t^{-1}), and an observation window of 10^6 steps corresponding to a time $T_{\text{obs}} = 10^4$ [32]. In order not to lose correlations due to methodological artifacts over the observation time, the time increment dt should become significantly smaller with growing T_{obs} . As it turns out, this makes the stochastic time evolution numerically highly demanding at ultra-low energies.

MaM: Generalized multifractal analysis (GMA). In order to explore $\varrho(E)$ at ultra-low energies, we first calculate the localization length, $\xi(E)$, with spectral methods which in turn is closely related to $\varrho(E)$: If one assumes that a localization volume ξ^2 has typically one state with lowest energy E_ξ one has: $|E_\xi| \xi^2 \varrho(E_\xi) = \mathcal{O}(1)$. Hence $\xi(E) \approx |E \cdot \varrho(E)|^{-1/2}$. The expression is familiar from the standard weak coupling analysis [7]. A complication arises because the same analysis predicts the form Eq. (1) for the DoS that turns out incompatible with our numerical data - as we already mentioned. Hence, a more general form $|E_\xi| \xi^2 \varrho(E_\xi) = r(\ell/\xi)$ should be considered (ℓ : a microscopic length). Partially inspired by most recent analytical work [16], we argue in the supplementary material that a reasonable assumption would be $r(X) \approx 1/X^\eta$ (with $\eta = 1$) at energies not too low, so that

$$\xi(E) \approx |E \cdot \varrho(E)|^{-1/(2+\eta)}. \quad (3)$$

Spectral methods allow us to extract the localization length even at very low energies and therefore can provide information about the DoS as well. Similar to Ref. [17], we employ a generalized multifractal analysis (GMA) for this purpose. It is motivated in the present context from the fact that multifractality at the Dirac-point is a topic of interest *per se*. The central observable is the inverse participation ratio (IPR), $P_q(E) = \int_{L^2} d\mathbf{r} |\psi_m(\mathbf{r})|^{2q}$, (For numerical efficiency, we average over a small number of

states with energies ϵ_m inside an interval about E . In addition, we also perform a disorder average - at fixed \bar{n} - that we indicate via \overline{P}_q .) To address the localization length, $\xi(E)$, one works at finite energies $|E| > 0$ in the vicinity of the critical fixed point where a scaling Ansatz

$$\overline{P}_q = L^{-\tau_q} \mathcal{F}_q(L/\xi(E)) \quad (4)$$

applies. We will extract $\xi(E)$ by scaling our numerical data according to this relation. The wavefunction data has been obtained in a well documented way (e.g. Ref. [18, 19]) employing standard sparse matrix routines [20].

Results: SCTMA. The DoS as obtained from the self-consistency cycle of the SCTMA is shown in Fig. 1 with dashed lines. In the limit of large and low energies we recover the expected qualitative behavior: If the energy exceeds a characteristic scale set by $\Delta(\bar{n}) = v_F \sqrt{\pi \bar{n} / \ln(n^*/\bar{n})}$, with $n^* = W^2 / \pi v_F^2$, and W a high-energy cut-off, [15], the DoS essentially remains unaffected by the impurities thus retaining the characteristic linear form reminiscent of clean graphene at high energies. (Our data suggests $n^* \approx 1$.) However, in the low-energy limit, $E \ll \Delta(\bar{n})$, the Dirac-singularity broadens and one obtains a constant value for the DoS.

As seen in the expression for the characteristic energy scale $\Delta(\bar{n})$, the SCTMA provides a logarithmic renormalization of the naive scale $\sqrt{\pi \bar{n} v_F^2}$ that follows from dimensional analysis. In similar vein, in the limit $E \rightarrow 0$, our data suggests that the saturation value of the DoS picks up similar logarithmic corrections, $\varrho^{\text{SCTMA}}(0) \sim \Delta(\bar{n}) \ln(n^*/\bar{n})$. Furthermore, this logarithmic dressing leads to the minimum in the DoS as seen in Fig. 1 [33].

Results, Tb-simulation: energy. Since the SCTMA ignores multiple scattering at two- (or more) impurity configurations, quantum-interference processes are absent. Hence, within the SCTMA one does not expect any indication of the E^{-1} singularity predicted in Eq. (1). To

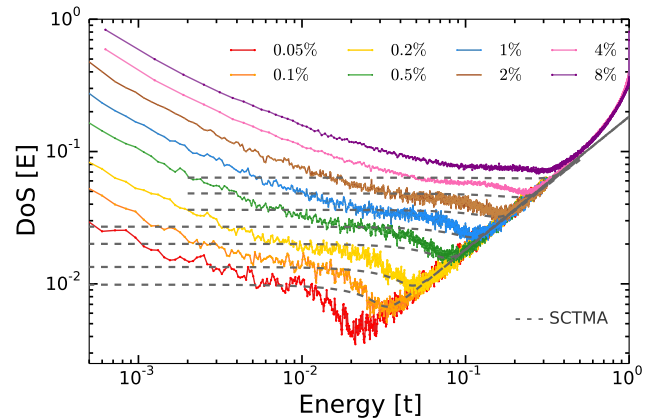


FIG. 1: (Color online) Density of states of graphene with $\bar{n}=0.1 - 8\%$ vacancies in either sublattice. Comparison of SCTMA and tight-binding simulation.

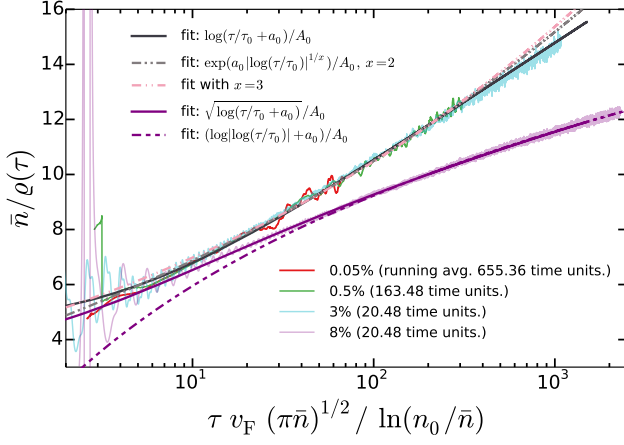


FIG. 2: (Color online) Data collapse of inverse time-series on a master curve, consistent with the Wegner-Gade scaling Eq. (1). Solid lines represent according fits: $\exp(a_0 |\ln(\tau/\tau_0)|^{1/x})/\mathfrak{A}_0$ ($x=2$: $(\tau_0, a_0, \mathfrak{A}_0) = (0.0169, 1.004, 1.838)$; $x=3/2$: $(0.00013, 0.614, 3.2)$) (Times τ_0 are measured in units $(\pi \bar{n} v_F^2)^{1/2} / \ln(n_0/\bar{n})$. We fix $n_0 \approx 2.08$ by collapsing onto the master curve.) Collapse restricts to a pre-asymptotic time window, $1 \ll \mathfrak{D}\tau \ll \mathfrak{D}\tau_n^*$ (displayed: $\bar{n} = 0.05\%, 0.5\%, 3\%$). After a crossover to ultra-long times, $\tau \gg \tau_n^*$, the increase of $\bar{n}/\rho(\tau)$ is sublinear; an example numerically accessible in this time regime is the $\bar{n} = 8\%$ -trace. We fit $\sqrt{\ln(\tau/\tau_0 + a_0)}/\mathfrak{A}_0$ ($(\tau_n, a_n, \mathfrak{A}_n) = (1.671, 1.74, 0.219)$) motivated by Ref. [16]. Dashed lines guide the eye indicating alternative fittings: $\ln(\tau)$ and $\ln \ln(\tau)$. The fluctuations in the raw data reflect the stochastic nature of the methodology.

investigate this, we resort to a numerical simulation of the DoS in the lattice model. As one might have suspected, the characteristic minimum in the DoS obtained within the SCTMA is also seen in the lattice simulation Fig. 1 and turns out to be even more pronounced there. Quantum interference becomes important at energies below a scale $\mathfrak{D}(\bar{n})$ where it gradually enhances the (upturning) curvature.

Results, Tb-simulation: time. At lowest energies the Fourier-transformation (FT) exhibits a sensitivity to the window of integration times. Even though artifacts are generally weak, for the present purpose we will work in the time representation and eliminate (residual) high-frequency contributions to $\rho(\tau)$ via running time averages (averaging windows: 20.48 - 655.36 time units); observation time $T_{\text{obs}} = 10^4$. Fig. 2 displays the first out of the two key results of this work: at intermediate times the DoS takes a form consistent with Eq. (1)

$$\rho(\tau) \approx \bar{n} \mathfrak{A}_0 \exp \left[-a_0 |\ln(\tau/\tau_0)|^{1/x} \right], \quad \mathfrak{D}^{-1} \ll \tau \ll \tau_n^*. \quad (5)$$

The crossover scale τ_n^* is very rapidly decreasing if \bar{n} grows from 3% to 10%. As a consequence, the onset of the ultra-long time regime can be investigated with the time propagation method. As shown in Fig. 3, at times

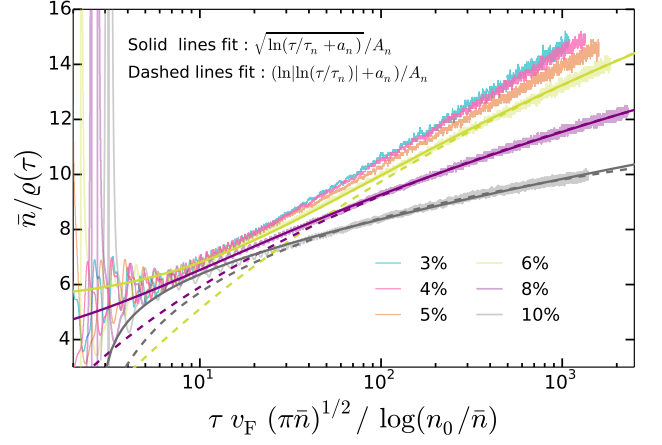


FIG. 3: (Color online) Evolution of $\bar{n}/\rho(\tau)$ into the ultra-long time regime. Concentrations: $\bar{n} = 3\%, 4\%, 5\%, 6\%, 8\%, 10\%$. Fits are indicated according to $\sqrt{\ln(\tau/\tau_n + a_n)}/\mathfrak{A}_n$ (solid): 6% : $(\tau_n, a_n, \mathfrak{A}_n) = (6.74, 2.27, 0.169)$; 8% : $(1.671, 1.74, 0.219)$; 10% : $(0.218, -11.76, 0.295)$ and $(\ln |\ln(\tau/\tau_n)| + a_n)/\mathfrak{A}_n$ (dashed): 8% : $(\tau_n, a_n, \mathfrak{A}_n) = (0.109, -0.77, 0.124)$; 10% : $(2.034, 1.425, 0.33)$.

exceeding τ_n^* the decay of $\rho(\tau)$ is much slower even than $1/\ln(\tau)$. The accessible time window is too small in order to reliably discriminate possible cases, $1 \leq \mathfrak{x} < 2$,

$$\rho(\tau) = \bar{n} \mathfrak{A}_n |\ln(\tau/\tau_n + a_n)|^{-\mathfrak{x}+1}, \quad \tau_n^* \ll \tau. \quad (6)$$

(Even $\mathfrak{x} \rightarrow 1$, i.e. $\rho(\tau) = \bar{n} \mathfrak{A}_n / (\ln(\ln(\tau/\tau_n)) + a_n)$, would not be incompatible with the data (see Figures 2 and 3).) What can safely be concluded at this point is that at very low energies $|E| \cdot \rho(E) \propto 1/\ln(|E|)^{\mathfrak{x}}$, $1 \leq \mathfrak{x} < 2$ at variance with Eq. (1).

Results: Generalized multifractal analysis We have calculated the IPR near four different energies covering the range $10^{-3}t - 10^{-7}t$. The resulting master curve \mathcal{F} defined in Eq. (4) is displayed in Fig. 4. In the regime of large system sizes $L \gg \xi(E)$ all curves exhibit a plateau indicating that the IPR is independent of the growing system size: we observe the insulating behavior expected for the AI-class that eventually governs all energies except $E=0$. At smaller $L/\xi(E)$ -values a power-law regime begins to develop that governs intermediate system sizes but is cut off at smallest values $L \ll \xi(E)$ where the slope begins to decrease again. This peculiar feature foreshadows the behavior at the critical fixed point. We believe that it indicates the existence of a second plateau in the limit $\xi \rightarrow \infty$ that exists at $q_c \leq q < 1$ and that is not yet fully developed in our data. This plateau is manifestation that certain moments, $q > q_c$, also of the critical wavefunctions become insensitive of the system size growth and are (in this sense) “frozen”.

Collapsing the IPRs on the master curve, Fig. 4, delivers τ_q and $\xi(E)$ in units of $\xi_0 \equiv \xi(E_0)$ for a reference energy E_0 . The multifractal spectrum τ_q is displayed in Fig. 4,

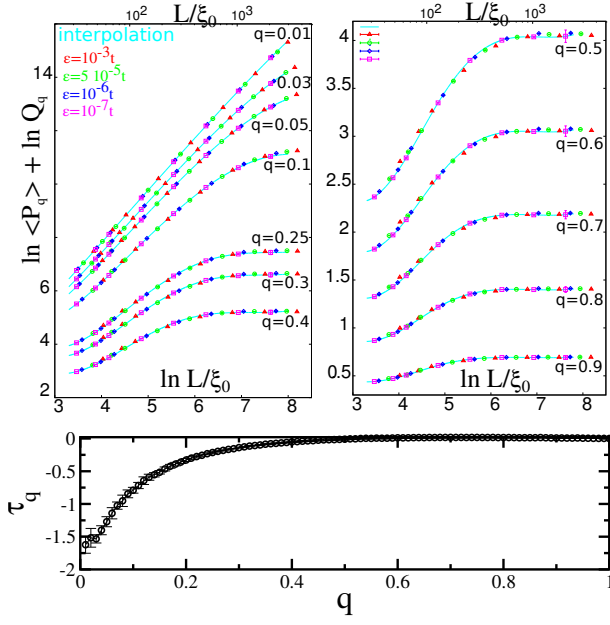


FIG. 4: (Color online) Top panels: master curves for different q -values as obtained after re-scaling of x, y -axes with energy-depending scale factors $\xi(E)$ (x -axis, depicted in Fig. 3) and $Q_q = \xi(E)^{\tau_q}$ (y -axis, not shown). Parameters: $\bar{n} = 4\%$, $L = 64, 128, 256, 512, 1024, 2048$, $\epsilon = 10^{-3}, 5 \times 10^{-5}, 10^{-6}, 10^{-7}$. IPR-distribution functions are given in the supplementary material. Bottom panel: multifractal spectrum as estimated from fitting to Q_q . It displays frozen multifractality.

lower panel. It supports the freezing scenario and gives a rough estimate $q_c \lesssim 0.5$. The localization length is shown in Fig. 5 and compared with the DoS-data converted into $\xi(E)$ via Eq. (3). (By matching both ξ -traces at $\epsilon=10^{-3}t$ we fix the GMA-scale ξ_0 .) The result is satisfactory in the sense that the matching procedure delivers a curve that smoothly interpolates from the high-energy (SCTMA) into the ultralow energy regime. This trace summarizes our second key statement. Namely, a consistent fit is achieved with $\eta=1$ and $\mathfrak{r} = 3/2$ over data spanning more than 5 orders of magnitude in energy. This result is in full agreement with the prediction by Ostrovsky *et al.* [16].

Conclusions: General implications. A first important conclusion from our numerical study is that the canonical σ -model of symmetry class BDI does not apply to the case of graphene with vacancies. One expects that the underlying reason is related to the fact that vacancies in the tight-binding representation should be understood as very strong (“unitary”) scatterers that enforce zero amplitude of the scattering wavefunction at the scattering center. In this sense the individual scatterer is never weak, which is at odds with the assumption underlying the derivation of the σ -model.

In principle, the observation that not only the symmetry class (here BDI), but also the type of disorder plays a crucial in determining the low-energy behavior has been made before [34]. Of particular interest here are

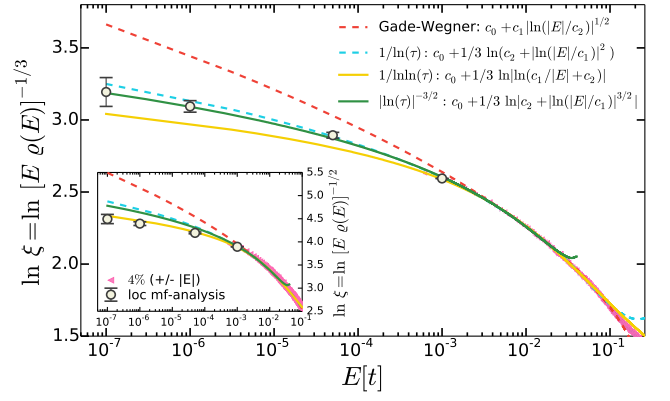


FIG. 5: (Color online) Localization length as obtained from the DoS (data Fig. 1. solid) and from the GMF-analysis (symbols, converted assuming $\eta=1$). Also shown are three fits to the high energy regime (see inset) that interpolate into the low energy section via FT of Eq. (5) (blue, Gade-Wegner-form, (2.192, 0.215, 1.6)) and Eq. (6) (yellow, $\mathfrak{r}=3/2$, (3.307, 0.0226, 1.0428)). [FT of Eqs. (1) ($\mathfrak{r}=2$, (c_0, c_1, c_2) = (0.1487, 1.0395, 0.285)) is also shown for comparison even though $\mathfrak{r}=2$ is already excluded from time series analysis.] Only Eq. (6) corresponding to $|E| \cdot \varrho(E) \sim 1/\ln(|E|)^{3/2}$ fits all regimes (with three fitting parameters). Inset: Conversion of DoS into $\xi(E)$ assuming $\eta=0$. Comparison illustrates that η indeed enters the data interpretation in an important way, since for $\eta=0$ only $\mathfrak{r}=1$ would provide an acceptable fit.

disordered d -wave superconductors with very strong scatterers. They belong to chiral class AIII, which is the unitary cousin of BDI. Its σ -model also exhibits the Gade-singularity, Eq. (1) [21]. In this context an interesting proposal deviating from the Gade-Wegner form has been made [22, 23] (e.g., $\varrho(E) \sim 1/|E \ln(E)|^2$, i.e. $\mathfrak{r}=2$ in our nomenclature), but so far its status has been controversial [35].

In a recent study [24], a very similar model, the Kitaev model that has a representation in terms of a bipartite random hopping problem of Majorana fermions on a hexagonal lattice in the background of Z_2 fluxes has been shown to have a similar singular DoS with $\mathfrak{r} \approx 1.7$. However, these results were obtained in the gapped phase of the model, wherein the isolated impurity states are exponentially localized- as opposed to a $1/r$ -envelop of vacancy induced zero modes in graphene. Hence, the relation of this result to graphene with vacancies is uncertain.

Conclusions: Microscopic realizations and graphene. From the point of view of graphene research, the relevance of our results depends on the applicability of the approximation of disorder as an ensemble of unitary scatterers. Such are realized at least approximately, e.g., when a carbon atom forms a chemical bond with an absorbate and therefore is taken from the sp^2 - into the sp^3 -hybridization. Indeed, an isolated sp^3 -hybrid induces a state typically of the order of 10meV away from midgap [5]. The zero-mode of the tight-binding vacancy should be understood

as an approximation for such a state. Correspondingly, we might expect that the structure of the DoS, that we study here, could be representative for the real material on the scale of several meV, i.e. well above $10^{-3}t$. Hence, the intermediate energy window, which displays the quantum interference enhanced increase of the DoS, should still be experimentally accessible, but the ultra-low energy range might prove difficult to reach.

Acknowledgments We thank J. Chalker, I. Gornyi, A. Mirlin, Chr. Mudry, H. Obuse and P. Ostrovsky for helpful discussions. Especially, we express our gratitude to I. Gornyi and P. Ostrovsky for sharing analytical results with us prior to publication. We acknowledge the DFG (CFN and SPP 1243) for financial support. We also thank I. Kondov and the Jülich Supercomputer Center (JUROPA, project HKA12) for computational assistance and resources.

-
- [1] A. H. Castro Neto, F. Guinea, N. M. R. Peres, K. S. Novoselov, and A. K. Geim, *Rev. Mod. Phys.* **81**, 109 (2009), URL <http://link.aps.org/doi/10.1103/RevModPhys.81.109>.
 - [2] V. M. Pereira, F. Guinea, J. M. B. Lopes dos Santos, N. M. R. Peres, and A. H. Castro Neto, *Phys. Rev. Lett.* **96**, 036801 (2006), URL <http://link.aps.org/doi/10.1103/PhysRevLett.96.036801>.
 - [3] V. M. Pereira, J. M. B. Lopes dos Santos, and A. H. Castro Neto, *Phys. Rev. B* **77**, 115109 (2008), URL <http://link.aps.org/doi/10.1103/PhysRevB.77.115109>.
 - [4] D. A. Abanin, A. V. Shytov, and L. S. Levitov, *Phys. Rev. Lett.* **105**, 086802 (2010), URL <http://link.aps.org/doi/10.1103/PhysRevLett.105.086802>.
 - [5] T. O. Wehling, S. Yuan, A. I. Lichtenstein, A. K. Geim, and M. I. Katsnelson, *Phys. Rev. Lett.* **105**, 056802 (2010), URL <http://link.aps.org/doi/10.1103/PhysRevLett.105.056802>.
 - [6] A. Altland and M. R. Zirnbauer, *Phys. Rev. B* **55**, 1142 (1997), URL <http://link.aps.org/doi/10.1103/PhysRevB.55.1142>.
 - [7] F. Evers and A. D. Mirlin, *Rev. Mod. Phys.* **80**, 1355 (2008), URL <http://link.aps.org/doi/10.1103/RevModPhys.80.1355>.
 - [8] R. Gade and F. Wegner, *Nucl. Phys. B* **360**, 213 (1991).
 - [9] R. Gade, *Nucl. Phys. B* **398**, 499 (1993).
 - [10] O. Motrunich, K. Damle, and D. A. Huse, *Phys. Rev. B* **65**, 064206 (2002).
 - [11] C. Mudry, S. Ryu, and A. Furusaki, *Phys. Rev. B* **64**, 064202 (2003).
 - [12] S. Yuan, H. De Raedt, and M. I. Katsnelson, *Phys. Rev. B* **82**, 115448 (2010), URL <http://link.aps.org/doi/10.1103/PhysRevB.82.115448>.
 - [13] T. Stauber, N. M. R. Peres, and A. H. Castro Neto, *Phys. Rev. B* **78**, 085418 (2008), URL <http://link.aps.org/doi/10.1103/PhysRevB.78.085418>.
 - [14] S. Wu, L. Jing, Q. Li, Q. W. Shi, J. Chen, H. Su, X. Wang, and J. Yang, *Phys. Rev. B* **77**, 195411 (2008), URL <http://link.aps.org/doi/10.1103/PhysRevB.77.195411>.
 - [15] P. M. Ostrovsky, I. V. Gornyi, and A. D. Mirlin, *Phys. Rev. B* **74**, 235443 (2006).
 - [16] P. M. Ostrovsky, I. V. Protopopov, E. J. König, I. V. Gornyi, A. D. Mirlin, and M. A. Skvortsov, arXiv:1404.6139 (2014).
 - [17] A. Rodriguez, L. J. Vasquez, K. Slevin, and R. A. Römer, *Phys. Rev. Lett.* **105**, 046403 (2010).
 - [18] F. Evers, A. Mildenberger, and A. D. Mirlin, *Phys. Rev. B* **64**, R241303 (2001).
 - [19] A. R. Subramaniam, I. A. Gruzberg, A. W. W. Ludwig, F. Evers, A. Mildenberger, and A. D. Mirlin, *Phys. Rev. Lett.* **96**, 126802 (2006).
 - [20] R. B. Lehoucq, D. C. Sorensen, and C. Yang, *ARPACK Users Guide: Solution of Large Scale Eigenvalue Problems by Implicitly Restarted Arnoldi Methods.* (1997).
 - [21] A. Altland, *Phys. Rev. B* **65**, 104525 (2002).
 - [22] C. Chamon and C. Mudry, *Phys. Rev. B* **63**, 100503 (2001).
 - [23] C. Pépin and P. A. Lee, *Phys. Rev. B* **63**, 054502 (2001), URL <http://link.aps.org/doi/10.1103/PhysRevB.63.054502>.
 - [24] A. J. Willans, J. T. Chalker, and R. Moessner, *Phys. Rev. B* **84**, 115146 (2011).
 - [25] S. Guruswamy, A. LeClair, and A. W. W. Ludwig, *Nucl. Phys. B* **583**, 475 (2000).
 - [26] V. Häfner, Diploma thesis, Karlsruhe Institute of Technology (2011).
 - [27] J. Schindler, Diploma thesis, Karlsruhe Institute of Technology (2012).
 - [28] P. J. Hirschfeld and W. A. Atkinson, *Jour. Low Temp. Phys.* **126**, 881 (2002).
 - [29] A. V. Balatsky, I. Vekhter, and J.-X. Zhu, *Rev. Mod. Phys.* **78**, 373 (2006).
 - [30] N. Weik, Diploma Thesis KIT (2013).
 - [31] The result was confirmed by Guruswamy et al. [25] in their analysis of a bipartite π -flux model that also belongs to class BDI. Specifically, this study shows that generic representatives of BDI exhibit a running coupling, $g_A \sim \ln L$. Within the π -flux model g_A has the interpretation of a coupling to a real random gauge-field. Since one has $z \approx 1 + 2g_A$, the previous conclusion $z(L) \sim \ln L$ is a consequence of “runaway flow”.
 - [32] At our system sizes, $L = 2048, 4096$, we did not observe a significant effect of ϕ -averaging on $\varrho(E)$ due to self-averaging. If not specified otherwise, averaging was over four initial states [26, 27]. A convergence test justifying the choice of dt is given in the supplementary material.
 - [33] Namely, the high energy trace follows the unperturbed behavior $\varrho(E) = |E|/\pi\sqrt{3}$ all the way down to $\Delta(\bar{n})$. At the departure point into the low-energy region, $\varrho(\Delta(\bar{n}))$ exhibits a DoS already below the limit $\varrho^{\text{SCTMA}}(0)$ and so the DoS increases again.
 - [34] For instance, symmetry class D: It allows for different lattice models (e.g. of the Chalker-Coddington type) that exhibit very different phase diagrams depending on the form of the disorder. Some may exhibit only (topologically different) localized phases (RBIM), but others may also support metallic phases (Cho-Fisher model). For a review see Ref. [7].
 - [35] For an overview, see e.g. Refs. [28, 29]

Supplementary material for “Density of states of graphene with vacancies: midgap power law and frozen multifractality”

We present technical details, such as analytical derivations and convergence tests, and additional data together with further arguments in support of the results reported in the main text. In the first part, we derive the DoS of graphene in the presence of compensated vacancy disorder using the SCTMA. In second part we provide details on convergence of the Krylov propagation method. Finally in the last section preliminary evidence of freezing transition in the IPR distribution of flow has been reported. Finally, we provide a heuristic argument about the fluctuation effects on the local density of states and its effect on the exponent η .

SELF-CONSISTENT T-MATRIX APPROXIMATION

In this section we briefly recall the selfconsistent T-matrix approximation for vacancy scattering in graphene.

Disorder Potential

A vacancy is a short-range impurity to be modeled by an impurity potential that mixes states only that within in the same sublattice as the vacancy [1, 2]. Let

$$\Psi = (\Psi_{A,K}, \Psi_{B,K}, \Psi_{B,K'}, \Psi_{A,K'})^T \quad (S1)$$

be the four-component wave-function in A, B -space of the sublattices and K, K' -valley space. In this representation the impurity potential of an impurity in sublattice A has the following shape [1, 2]

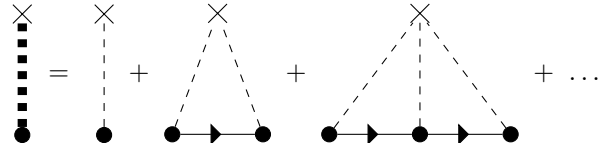
$$V_k^A(r) = \begin{pmatrix} V_0 & 0 & 0 & V_0 e^{-2i\mathbf{k}_0 \cdot \mathbf{r}} \\ 0 & 0 & 0 & 0 \\ 0 & 0 & 0 & 0 \\ V_0 e^{2i\mathbf{k}_0 \cdot \mathbf{r}} & 0 & 0 & V_0 \end{pmatrix} \cdot e^{-i\mathbf{k} \cdot \mathbf{r}}, \quad (S2)$$

where $\mathbf{k}_0 = \mathbf{K} - \mathbf{K}'$ and V_0 is proportional to the impurity potential V [2]. Accordingly, the scattering potential for an impurity in sublattice B [2] is given by

$$V_k^B(r) = \begin{pmatrix} 0 & 0 & 0 & 0 \\ 0 & V_0 & V_0 e^{-2i\mathbf{k}_0 \cdot \mathbf{r}} & 0 \\ 0 & V_0 e^{2i\mathbf{k}_0 \cdot \mathbf{r}} & V_0 & 0 \\ 0 & 0 & 0 & 0 \end{pmatrix} \cdot e^{-i\mathbf{k} \cdot \mathbf{r}}. \quad (S3)$$

Selfconsistent T-Matrix Approximation

The *T-matrix approximation* for impurity scattering entails the neglect of all diagrams with crossing of impurity lines [3, 4]. The T matrix can be expressed as the following geometric series of diagrams [2–4]



$$= \text{[Diagram 1]} + \text{[Diagram 2]} + \text{[Diagram 3]} + \dots \quad (S4)$$

The usual diagrammatic notation is applied where crosses denote scattering off the impurity with potential V and the propagators denote the bare Green's function [2, 3].

$$G_0(\epsilon, k) = \frac{\epsilon + v_F \tau_3 \sigma \cdot \mathbf{k}}{\epsilon^2 - v_F^2 k^2}. \quad (S5)$$

Evaluating the geometric series one obtains

$$T = V \sum_{n=0}^{\infty} (G_0 V)^n = \frac{V}{1 - G_0 V} \xrightarrow{V \rightarrow \infty} \frac{1}{G_0}, \quad (\text{S6})$$

and the T -matrix becomes independent of the of the impurity strength in the unitary limit that resembles the vacancies [2, 5]. When replacing G_0 by the full Green's function [2]

$$G(\epsilon, k) = \frac{\epsilon + v_F \tau_3 \sigma \cdot \mathbf{k}}{(\epsilon - \Sigma(\epsilon, k))^2 - v_F^2 k^2}, \quad (\text{S7})$$

the *selfconsistent T-matrix approximation* is obtained, where Σ denotes the particles' self-energy in the presence of impurities [3, 4]. Performing a disorder-average for Σ w.r.t. the position of the vacancies the self-energy is approximated by n_{vac} -times the disorder-averaged T -matrix. The disorder- average is performed separately for the vacancies in the A - and in the B -sublattice in k -space representation following to Ref. [6]:

$$\begin{aligned} \langle \Sigma(\epsilon) \rangle &= \begin{pmatrix} \langle \Sigma_A(\epsilon) \rangle & 0 \\ 0 & \langle \Sigma_B(\epsilon) \rangle \end{pmatrix} \\ &= \begin{pmatrix} n_A \langle T_A(\epsilon) \rangle & 0 \\ 0 & n_B \langle T_B(\epsilon) \rangle \end{pmatrix}. \end{aligned} \quad (\text{S8})$$

Note that n_A and n_B denote the density of impurities w.r.t. the total number of carbon atoms in the sample:

$$n_{(A/B)} = \frac{N_{(A/B)}}{N_{\text{sites}}}$$

(Here, we employ the convention of the SCTMA-literature where $n_{A/B}$ denotes the fraction of A/B -vacancies with respect to all lattice sites. With this convention the total concentration of vacancies is given by $\bar{n} = n_A + n_B$.)

Making use of identity Eq. (S6) we derive a set of interdependent equations,

$$\langle T \rangle = \begin{pmatrix} \langle T_A \rangle & 0 \\ 0 & \langle T_B \rangle \end{pmatrix} = \frac{1}{\langle G(\epsilon) \rangle} \quad (\text{S9})$$

$$\langle \Sigma(\epsilon) \rangle = \begin{pmatrix} n_A \langle T_A(\epsilon) \rangle & 0 \\ 0 & n_B \langle T_B(\epsilon) \rangle \end{pmatrix} \quad (\text{S10})$$

$$\begin{aligned} \langle G(\epsilon) \rangle &= \int \frac{d^2 k}{(2\pi)^2} G(\epsilon, k) \\ &= -\frac{1}{2\pi v_F^2} \log \left(1 - \frac{W^2}{\varepsilon_A \varepsilon_B} \right) \begin{pmatrix} \varepsilon_B & 0 \\ 0 & \varepsilon_A \end{pmatrix}, \end{aligned} \quad (\text{S11})$$

which require selfconsistent solution [6]. Here, the abbreviation [6]

$$\varepsilon_A = \epsilon - \langle \Sigma_A(\epsilon) \rangle; \quad \varepsilon_B = \epsilon - \langle \Sigma_B(\epsilon) \rangle \quad (\text{S12})$$

has been used; $W \equiv 3t$ denotes the bandwidth of the π -band and v_F is the Fermi energy. We further note that as shown in [2], this non-crossing expansion breaks down below an energy scale $\Delta(\bar{n}) = v_F \sqrt{\pi \bar{n} / \ln(n^*/\bar{n})}$. As usual, the density of states can be determined from $\langle G \rangle$ via [2, 3]

$$\rho(\epsilon) = -\frac{1}{\pi} \Im \left(\text{tr}(\langle G(\epsilon - i0) \rangle) \right). \quad (\text{S13})$$

(When comparing to numerical data from the Krylov space simulation, the SCTMA-result has to be multiplied by a factor of 2 reflecting the existence of two Dirac points in the lattice model.)

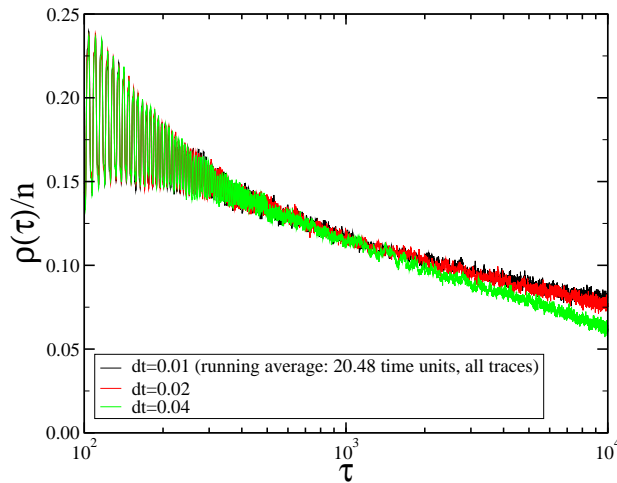


FIG. S1: (Color online) The Fourier-transformed, $\varrho(\tau)$, of the density of states ($\varrho(E)$) as obtained from the stochastic representation Eq. (2) via Krylov-time-propagation for an impurity concentration $\bar{n} = 0.5\%$.

CONVERGENCE TEST FOR KRYLOV PROPAGATION

The Krylov propagation method has two important parameters, the size of the Krylov space, N_{Krylov} , and the time increment dt . For computational efficiency one would like to take dt as large as possible while at the same time keeping N_{Krylov} small. In all our calculations we have chosen $N_{\text{Krylov}} = 4$. Fig. 2 provides evidence that with this choice a setting $dt = 0.01t$ is sufficient. The traces indicate that there is a time scale associated with each value of dt such that beyond that scale the correlation function $\varrho(\tau)$ decays too fast. For instance, with $dt = 0.04$ (Fig. S1, green) this scale is well below the observation time $T_{\text{obs}} = 10000$. On the other hand, the traces for $dt=0.01$ (black) and $dt=0.02$ (red) overlap very well within this time window. The situation is completely analogous for all other concentrations as well. For this reason we consider our choice $dt=0.01$ for the time increment as sufficiently conservative.

Moreover, we emphasize that computational artifacts related to time propagation tend to enhance the decay of correlations. Since our numerical calculations indicate an unexpectedly *slow* decay, however, we believe that this aspect of time propagation is very reliable.

FLOW OF THE IPR-DISTRIBUTION FUNCTION AND FREEZING

At a critical point the distribution function of the (logarithm of the) inverse participation ratio exhibits a simple scaling property: it flows homogeneously with increasing system size, L , without changing its shape. As seen in Fig. S2 there is no such homogeneous flow near the Dirac point. The behavior is expected at larger system sizes, where conventional localization sets in so that the distribution function becomes independent of the system size and the flow stops. Unexpected is, that the window of system sizes at which $L \ll \xi(E)$ remains very narrow even when decreasing the observation energies by three orders of magnitude from 10^{-3} down to $10^{-6}t$. By consulting Fig. S2 convinces oneself that the evolution of the overall flow changes extremely slowly upon approaching the Dirac point at zero energy consistent with the almost flat shape of $\xi(E)$ displayed in Fig. 5 at ultra-low energies.

Remarkably, the strongest changes in the flow are visible at values $q \lesssim 1$. Here, flow-modifications exist with decreasing the energy in the realm of small system sizes, e.g., clearly visible at $q = 0.15, 0.25, 0.4$. By contrast, there are significantly less modifications at $q > 1$ in this regime, comparing e.g. $q = 0.4$ and $q = 1.5$. We take this as preliminary evidence for the presence of freezing of the IPR which would correspond to $\tau_q=0$ at $q > 1$ at strictly zero energy.

FLUCTUATION EFFECTS IN THE LOCAL DENSITY OF STATES: EXPONENT η

We propose a simple heuristic argument indicating that a wide region of energies exist for which the typical number of states in the localization volume behaves like $(\sqrt{\bar{n}}\xi)^{-\eta}$ with $\eta=1$. To this end we consider a graphene flake of size

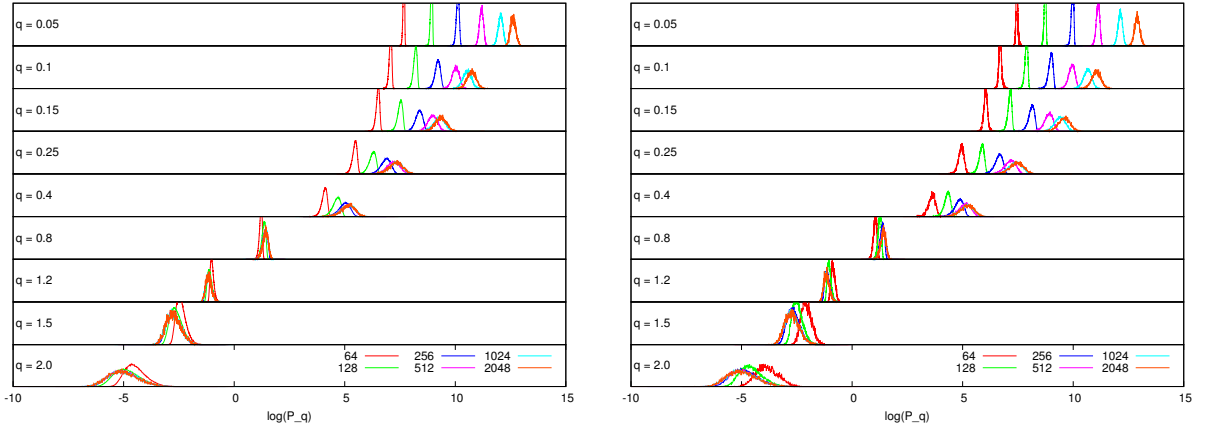


FIG. S2: (Color online) The flow of the distribution function of the inverse participation ratio (IPR) for linear system sizes $L = 64, 128, 256, 512, 1024, 2048$ at energies 10^{-3} (upper panel) and 10^{-6} (lower panel) for selected q -values. The flow of the average value with system size is captured by the scaling function $\mathcal{F}(L/\xi(E))$ defined in Eq. (4) and displayed in Fig. 5.

L^2 . We cover it with boxes of size λ^2 where $L \gg \lambda \gg \ell$ and ℓ is a microscopic length. Each box contributes on average a number of states

$$Z(\lambda, E) = \lambda^2 \int_0^E dE' \varrho(E') \sim \lambda^2 E \varrho(E). \quad (\text{S14})$$

with energy in the interval $(0, E]$. Suppose that ϵ is the typical value for the smallest energy that a box contributes.

For weak scatterers (Gaussian disorder) we would expect that ϵ is of the order of the level spacing

$$\Delta_\lambda = [\lambda^2 \varrho(\Delta_\lambda)]^{-1} \quad (\text{S15})$$

with fluctuations of order unity. However, vacancies do not appear to fall into this class.

Indeed, consider the fluctuations of the mismatch of the number of vacancies per sublattice in each box, $\delta n = \sqrt{(N_A - N_B)^2}$; we have $\delta n^2 \approx 2\bar{n}\lambda^2$. Now, a mismatch δn is associated with a spectral gap $E_{\text{gap}} \sim \eta v_F \sqrt{\bar{n}}$, $\eta = \delta n / \bar{n}$. On SCTMA-level (ignoring possible logarithmic corrections [30]) we get the estimate $E_{\text{gap}}(\lambda) \sim v_F / \lambda$. Therefore, most boxes exhibit a spectral gap that is much larger than the mean level spacing: $E_{\text{gap}}(\lambda) \gg \Delta_\lambda$. Only a small fraction of all boxes, $r(\lambda)$, can contribute to the total DoS at energies below the gap $E_{\text{gap}}(\lambda)$. We assume, that only those boxes contribute that have a nearly vanishing mismatch. This implies that $r(\lambda) \approx 1/\sqrt{\bar{n}\lambda^2}$. To restore the correct global average, the effective DoS in this residual subset of all boxes should be enhanced: $\varrho_{\text{eff}}(E) = \varrho(E)/r(\lambda)$.

Consequences for the localization length. For Gaussian disorder all boxes contribute to the DoS in a similar way. We expect a relation for the localization length to the average spectral gap: $Z(\xi, \Delta_\xi) \approx \mathcal{O}(1)$ with $\Delta_\xi \approx \epsilon$. As we just have seen, for the case of vacancies the DoS states in those boxes that contribute at very low energies is renormalized. We extract a localization length from these boxes declaring that

$$\xi^2(\epsilon) \epsilon \varrho_{\text{eff}}(\epsilon) \approx \mathcal{O}(1) \quad (\text{S16})$$

implying $r(\xi) \sim 1/\sqrt{\bar{n}\xi^2}$ and $\eta=1$.

-
- [1] T. Ando, Y. Zheng and H. Suzuura, J. Phys. Soc. Jpn. **71**, 1318 (2002).
 - [2] P. M. Ostrovsky, I. V. Gornyi and A. D. Mirlin, Phys. Rev. B **74**, 235443 (2006).
 - [3] B. Yu-K. Hu, E. Hwang and S. D. Sarma, Phys. Rev. B. **78**, 165411 (2008).
 - [4] A. Altland and B. Simons, Condensed matter field theory (CUP) (2006).
 - [5] G. D. Mahan, Many-particle physics (Springer) (2000).
 - [6] D. A. Abanin, A. V. Shytov and L. S. Levitov, Phys. Rev. Lett **105**, 086802 (2010).